Journal of Electronics, Electromedical Engineering, and Medical Informatics
Homepage: jeeemi.org; Vol. 9, No. 1, January 2027, pp: 15-32 e-ISSN: 2656-8632

RESEARCH ARTICLE OPEN ACCESS

AEPS-PINN: Adaptive Energy-Prior Scheduling with Superposed Multi-Harmonic Excitation for Physics-Informed Electrical Impedance Tomography

Dikky Juliyanto, and Endah Rahmawati

Department of Physics, Universitas Negeri Surabaya, Surabaya, Indonesia

Corresponding author: Endah Rahmawati (e-mail: endahrahmawati@unesa.ac.id), **Author(s) Email**: Dikky. J. (e-mail: dikky.23108@mhs.unesa.ac.id)

Abstract

Background: Electrical Impedance Tomography (EIT) reconstructs internal conductivity distributions from boundary voltage measurements, but its ill-posed nature and limited sensitivity to interior structures remain major challenges.

Aims: This study develops and evaluates AEPS-PINN, a physics-informed reconstruction framework incorporating Adaptive Energy-Prior Scheduling to reduce the computational overhead of energy-based regularization.

Methods: The framework combines superposed multi-harmonic excitation, a dual-head Physics-Informed Neural Network (PINN) for electric potential and conductivity estimation, and an Energy-Based Model (EBM) prior activated selectively when the governing partial differential equation residual exhibits stagnation. Training employs Adam optimization followed by L-BFGS refinement.

Results: Performance was evaluated using a synthetic three-inclusion conductivity phantom under identical optimization budgets for Standard PINN, Static EBM-PINN, and AEPS-PINN configurations. AEPS-PINN achieved a mean squared error (MSE) of 0.9008 (n = 5), compared with 0.9127 (n = 4) for Standard PINN and 0.8967 (n = 5) for Static EBM-PINN, with no statistically significant improvement over Standard PINN under the Wilcoxon signed-rank test. The adaptive scheduler reduced EBM evaluations by approximately 99.8%, from 7,511 ± 353 to 15 ± 4 evaluations per run, without a measurable deterioration in reconstruction accuracy. However, Dice and Intersection-over-Union scores remained zero across all configurations, indicating unsuccessful spatial recovery of the conductivity inclusions. Furthermore, the superposed multi-harmonic excitation produced a rank-1 boundary-voltage response matrix, corresponding to a single independent current-injection pattern rather than four separately applied patterns.

Conclusion: These findings demonstrate that AEPS-PINN substantially reduces energy-prior evaluation requirements while maintaining reconstruction performance comparable to continuously regularized PINN. Nevertheless, reliable inclusion recovery requires more informative boundary measurements, particularly multiple independent current-injection patterns, followed by experimental validation.

Keywords Electrical Impedance Tomography; Physics-Informed Neural Networks; Adaptive Energy-Prior Scheduling; Energy-Based Model; Conductivity Reconstruction.

I. Introduction

Electrical Impedance Tomography (EIT) reconstructs the internal conductivity distribution of an object from boundary voltage measurements [1], [2]. Although it is non-invasive, low-cost, and suitable for repeated biomedical monitoring [3], EIT is severely ill-posed: small measurement perturbations produce large uncertainty in the estimated conductivity, and the distinguishability of interior structures decreases with distance from the boundary [4], [5]. Recovering inclusions located away from the electrodes therefore remains a central challenge. Classical approaches address this ill-posedness through regularized iterative reconstruction, as implemented in EIDORS [6] and GREIT [7], with total-variation regularization to preserve sharp boundaries [8] and the complete electrode model to describe the measurement physics [9]. These methods rely on multiple current-injection patterns, because the reconstructable information

Manuscript received 14 August 2026; Accepted 16 October 2026; Available online 9 November 2026
Digital Object Identifier (**DOI**): https://doi.org/10.35882/jeeemi.v9i1.2012
Copyright © 2026 by the authors. This work is an open-access article and licensed under a Creative Commons Attribution-ShareAlike 4.0 International License (CC BY-SA 4.0).

depends on the number and choice of the applied patterns [4], [10]. Data-driven methods have since been introduced for inverse imaging [11], [12], [13], including CNN post-processing of D-bar reconstructions [14], [15], organ-boundary recovery [16], and networks built on direct sampling methods [17], as reviewed in [18].

Physics-Informed Neural Networks (PINNs) instead embed the governing equation directly in the training objective [19]. In EIT, PINN-type formulations have been applied to forward, semi-inverse, and full-inverse problems [20], composite sensing [21], real-time dynamic imaging [22], hybrid CNN–PINN full-inverse reconstruction [23], [24], and lung imaging [25], although their effectiveness depends strongly on gradient quality and loss balance [26]. Pokkunuru *et al.* improved PINN convergence for EIT by adding a pretrained energy-based model (EBM) [27] as a Bayesian prior [28]. This prior, however, is evaluated at every optimization step, so its cost scales with the full training budget regardless of whether it contributes useful information; moreover, as noted by Yang *et al.*, existing PINN approaches to EIT rely on internal potential data that are unavailable in boundary-only measurements [24].

Two research gaps follow. First, learned priors in PINN-based EIT are applied continuously, and whether a prior is actually needed during optimization has not been examined. Second, although classical theory links reconstructable information to the number of current patterns [4], [10], the information content of the excitation used in PINN-based EIT is rarely measured, making it difficult to attribute reconstruction failures to the method or the measurement. This study therefore proposes AEPS-PINN (Adaptive Energy-Prior Scheduling PINN). Unlike the continuously applied prior of Pokkunuru *et al.*, the EBM in AEPS-PINN is activated only when a scheduler detects stagnation of the PDE residual. The framework combines this scheduler with superposed multi-harmonic excitation and a dual-head PINN with Fourier feature encoding [29], [30] and a bounded conductivity output trained through a straight-through estimator [31], optimized by Adam [32] followed by L-BFGS [33], within a controlled computational setting that includes an idealized background anchor.

This study aims to develop a stagnation-gated prior-scheduling framework for PINN-based EIT and, under equal optimization budgets, evaluate both its computational behavior and the extent to which interior conductivity can be recovered from a single-injection boundary measurement. The contributions are fivefold: (1) a superposed multi-harmonic excitation strategy, with a rank analysis showing that superposition increases the boundary-signal amplitude by a factor of 1.99 without increasing the measurement rank; (2) an analytical characterization of radial sensitivity decay; (3) analysis and numerical verification of two gradient limitations, namely the smooth Born-kernel gradient at uniform conductivity and error accumulation in differentiable Jacobi relaxation; (4) the AEPS-PINN framework, which applies the energy prior adaptively rather than continuously; and (5) a controlled five-seed evaluation establishing that no configuration recovers the inclusions, a failure that may be associated with the limited excitation diversity of a single current-injection pattern, although other methodological factors may also contribute. Section II presents the methodology, Section III the results, Section IV the discussion, and Section V the conclusion.

II. Method

The EIT inverse problem is formulated on a bounded domain Ω with boundary $\partial\Omega$, where the conductivity $\sigma(x, y)$ is recovered from boundary measurements [1], [2]. The electric potential $u(x, y)$ satisfies the elliptic conductivity equation of Eq. (1) [1], [2] with the Neumann condition of Eq. (2) [1], [34] for a prescribed current pattern $g(\theta)$, where n is the outward unit normal:

$$-\nabla \cdot (\sigma \nabla u) = 0, \quad \text{in } \Omega \tag{1}$$

$$\sigma \frac{\partial u}{\partial n} = g(\theta), \quad \text{on } \partial\Omega \tag{2}$$

The boundary response is described by the Dirichlet-to-Neumann (DtN) map Λ_σ in Eq. (3) [2], whose dependence on σ carries the information available for reconstruction. For the unit disk with homogeneous conductivity σ_0, the harmonic modes $\cos(m\theta)$ are eigenfunctions of the DtN map, Eq. (4) [10], [34], and a perturbation at radius r_0 affects the m-th mode in proportion to r_0^{2m}, Eq. (5) [4], [5], where $S_m(r_0)$ is the sensitivity of mode m. Eq. (5) expresses the depth-dependent loss of distinguishability of boundary data.

$$\Lambda_\sigma : u|_{\partial\Omega} \mapsto \sigma \frac{\partial u}{\partial n}|_{\partial\Omega} \tag{3}$$

$$\Lambda_{\sigma_0}[\cos(m\theta)] = \sigma_0 \, m\cos(m\theta) \tag{4}$$

$$\frac{S_m(r_0)}{S_m(1)} = r_0^{2m} \tag{5}$$

In the PINN formulation [19], [35], u and σ are represented by neural networks trained to minimize the residual of Eq. (1), defined at interior points by Eq. (6) [19], [20] and computed by automatic differentiation [36], together with the boundary, measurement, and prior terms of Section II.D. The overall framework is shown in Fig. 1.

$$r(x, y) = -\nabla \cdot \big(\sigma(x, y)\nabla u(x, y)\big) \tag{6}$$

Manuscript received 14 August 2026; Accepted 16 October 2026; Available online 9 November 2026
Digital Object Identifier (**DOI**): https://doi.org/10.35882/jeeemi.v9i1.2012
Copyright © 2026 by the authors. This work is an open-access article and licensed under a Creative Commons Attribution-ShareAlike 4.0 International License (CC BY-SA 4.0).

A. EIT Forward Problem and Multi-Harmonic Excitation

For homogeneous σ_0 and a Neumann pattern $g(\theta)$ on the unit disk $\Omega = \{(r, \theta): 0 \le r < 1\}$, the forward solution admits the Fourier expansion of Eq. (7) [1], [34], where a_m and b_m are the Fourier coefficients of $g(\theta)$. The superposed excitation combines the first four cosine modes with amplitudes $a_1 = 0.6$, $a_2 = 0.4$, $a_3 = 0.25$, and $a_4 = 0.15$, Eq. (8) [4], [10], so that the homogeneous solution and its boundary trace are given by Eq. (9) [1] and Eq. (10) [1], [10], respectively.

$$u(r,\theta) = \sum_{m=0}^{\infty} [a_m r^m \cos(m\theta) + b_m r^m \sin(m\theta)] \quad (7)$$

$$g(\theta) = \sum_{m=1}^{4} a_m \cos(m\theta) \quad (8)$$

$$u_h(r,\theta) = \sum_{m=1}^{4} a_m r^m \cos(m\theta) \quad (9)$$

$$u_h(1,\theta) = \sum_{m=1}^{4} a_m \cos(m\theta) \quad (10)$$

Measured on the evaluation phantom over 256 boundary points, the RMS boundary amplitude is 0.904 for the superposed excitation and 0.454 for a single $m = 2$ excitation with $a_2 = 0.4$, a gain of 1.99. Section III.E shows that this gain is not accompanied by an increase in the rank of the measurement data.

B. Sensitivity Analysis and Gradient Limitations

For a compactly supported perturbation $\delta\sigma$ centered at (r_0, θ_0) with $r_0 < 1$, the Born approximation gives the change in the m-th boundary Fourier coefficient as Eq. (11) [2], [37], so that the modal sensitivity scales as Eq. (12) [4], [5].

$$\delta u_m \approx -\frac{a_m^2}{\sigma_0} r_0^{2m} \cos^2(m\theta_0)\, \delta\sigma(r_0,\theta_0) \quad (11)$$

$$S_m(r_0) = \frac{\delta u_m}{\delta\sigma} \propto a_m^2\, r_0^{2m} \quad (12)$$

The sensitivity therefore decays as r_0^{2m}, most rapidly for the higher modes (Fig. 2). The aggregate sensitivity of an N-mode excitation is given by Eq. (13) [5], [10].

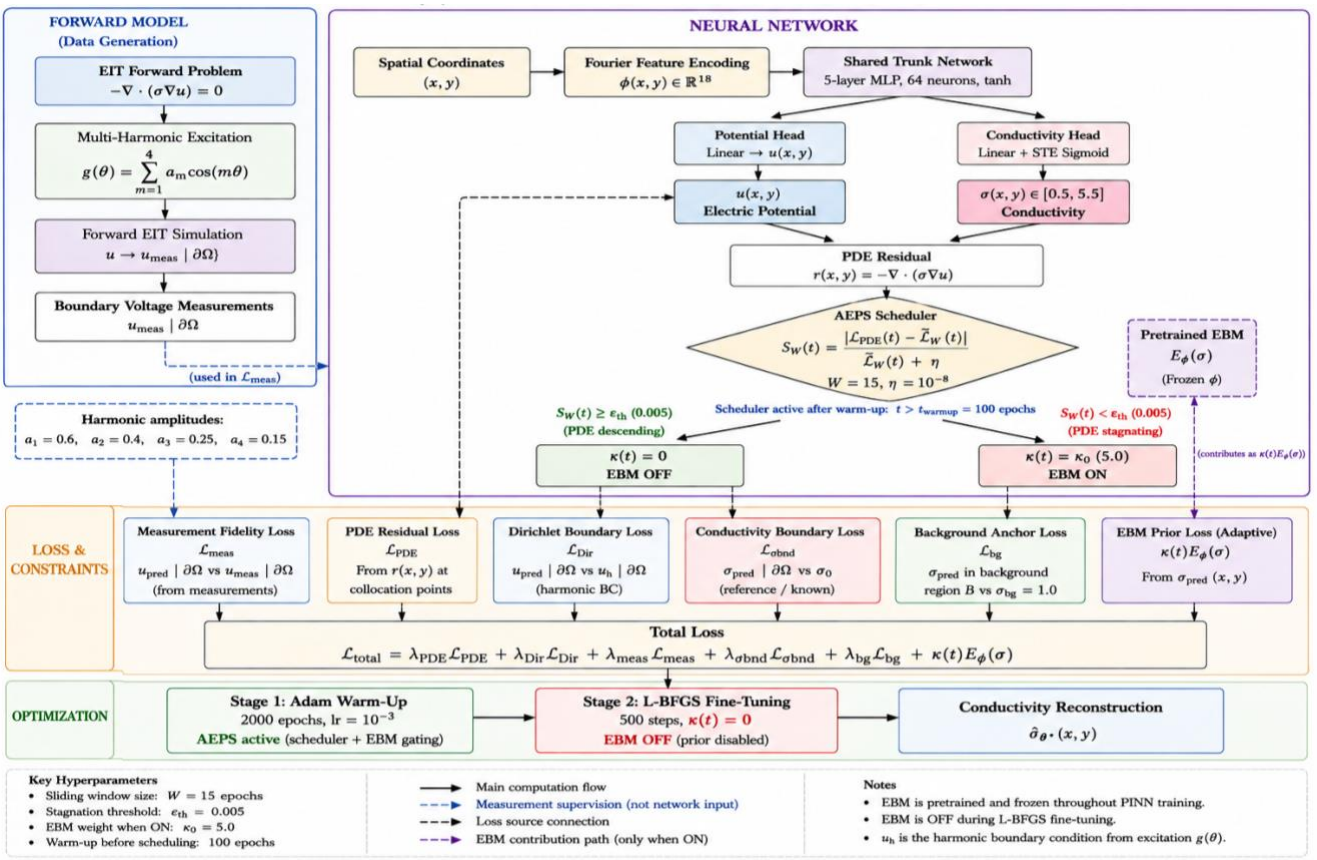


Fig. 1. Overall architecture of the AEPS-PINN framework illustrating multi-harmonic EIT data generation, Fourier feature encoding, dual-head neural-network prediction, adaptive EBM regularization, composite loss calculation, and two-stage optimization.

Manuscript received 14 August 2026; Accepted 16 October 2026; Available online 9 November 2026
Digital Object Identifier (**DOI**): https://doi.org/10.35882/jeeemi.v9i1.2012
Copyright © 2026 by the authors. This work is an open-access article and licensed under a Creative Commons Attribution-ShareAlike 4.0 International License (CC BY-SA 4.0).

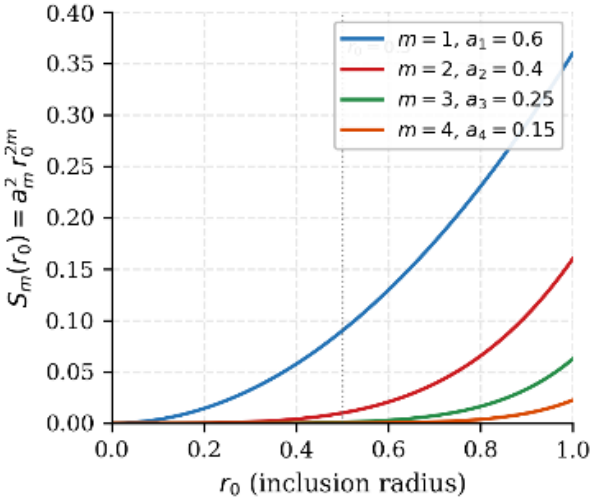
$$S_{\text{total}}(r_0) = \sum_{m=1}^{N} a_m^2 \, r_0^{2m} \tag{13}$$

For N = 4 and the amplitudes above, Eq. (13) gives $S_{\text{total}}(\ 0.5) = 0.101$, whereas a single m = 2 mode gives $S_2(0.5) = a_2^2 r_0^4 = 0.0100$, a ratio of 10.1.

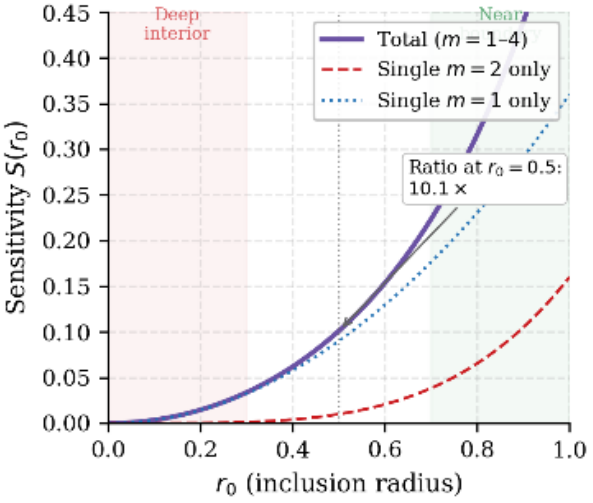
Proposition 1 (Born-kernel gradient at uniform conductivity). At $\sigma(x, y) = \sigma_0$, the adjoint gradient $\partial L_{\text{fwd}}/\partial\sigma(x, y)$ of the forward-consistency loss $L_{\text{fwd}} = \Sigma_m \delta_m^2$, where δ_m is the residual of the m-th boundary and inclusion radii of up to 0.245, the r^{2m} law is only a qualitative trend here: the measured decay exponents on the phantom are 1.23, 1.86, 2.89, and 2.34 for m = 1–4, below the theoretical value of $2m$.

Proposition 2 (Jacobi backward accumulation error). When the gradient of the boundary-data loss is computed through K differentiable Jacobi sweeps, the accumulated numerical error grows with K.

Analysis. The Jacobi update of the discretized forward problem is Eq. (16) [38], where $j \sim i$ denotes the four neighbouring grid points and $\sigma_i = \sigma(x_i, y_i)$. After K sweeps, $u^{(K)} = \Phi^K(u^{(0)})$, where Φ is the Jacobi operator, and the Jacobian with respect to σ decomposes by the chain rule of reverse-mode differentiation as in Eq. (17) [36]. Each factor $\partial\Phi/\partial u^{(j)}$ is sparse with entries of magnitude $O(1)$, so the worst-case floating-point error accumulates linearly, Eq. (18) [39].



(a) Individual Mode Sensitivities



(b) Total vs Single-Mode Sensitivity

Fig. 2. Radial sensitivity analysis of harmonic excitation in electrical impedance tomography: (a) sensitivity of individual harmonic modes (m = 1–4) and (b) aggregated sensitivity of superposed multi-harmonic excitation as a function of inclusion radius. Here, r_0 denotes the radial position of the inclusion, the mode amplitudes are a_1–a_4 = 0.6, 0.4, 0.25, 0.15, and panel (b) also compares the aggregated sensitivity with single-mode excitation (m = 1 or m = 2 only), giving a ratio of 10.1 relative to the m = 2 mode at r_0 = 0.5.

Fourier coefficient, is a smooth spatial function without inclusion-to-background contrast.

Analysis. Differentiating L_{fwd} with the sensitivity of Eq. (11) gives the adjoint gradient of Eq. (14) [2], [37], and substituting the modal solution $u_m = a_m r^m \cos(m\theta)$ of Eq. (9) gives Eq. (15) [37].

$$g(x, y) = -\frac{2}{\sigma_0} \sum_{m} \delta_m \, u_m(x, y)^2 \tag{14}$$

$$g(r, \theta) = -\frac{2}{\sigma_0} \sum_{m=1}^{N} \delta_m \, a_m^2 \, r^{2m} \cos^2(m\theta) \tag{15}$$

The gradient is a superposition of the smooth functions $r^{2m}\cos^2(m\theta)$, which carry no inclusion boundary; at uniform conductivity it therefore provides no inclusion-to-background contrast. Because the Born approximation assumes weak contrast and small perturbations, whereas the phantom has a 5:1 contrast

$$u_i^{(k+1)} = \frac{1}{4\sigma_i} \sum_{j \sim i} \sigma_j \, u_j^{(k)} \tag{16}$$

$$\frac{\partial u^{(K)}}{\partial \sigma} = \sum_{k=0}^{K-1} \left(\prod_{j=k+1}^{K-1} \frac{\partial \Phi}{\partial u^{(j)}} \right) \frac{\partial \Phi}{\partial \sigma} \Big|_{u^{(k)}} \tag{17}$$

$$\epsilon_K = \sum_{k=0}^{K-1} O\,(1)^{K-k-1} \epsilon_{\text{round}} = O(K)\, \epsilon_{\text{round}} \tag{18}$$

Manuscript received 14 August 2026; Accepted 16 October 2026; Available online 9 November 2026
Digital Object Identifier (**DOI**): https://doi.org/10.35882/jeeemi.v9i1.2012
Copyright © 2026 by the authors. This work is an open-access article and licensed under a Creative Commons Attribution-ShareAlike 4.0 International License (CC BY-SA 4.0).

Direct verification by automatic differentiation shows that the error grows with K as predicted (fitted exponent 0.90 for K = 50–300) but remains far below the worst-case bound: 9.8×10^{-10} at K = 300 versus 3×10^{-5} from Eq. (18). For $K \geq 100$, the autodiff gradient deviates from a float64 reference by less than 0.5% (relative L2) with a cosine similarity of 1.0000. In the implementation, the forward-consistency weight is $\lambda_{\text{fwd}} = 0$, so the differentiable solver is not evaluated during training, and the boundary data are produced by a separate non-differentiable solve with 5,000 sweeps. Proposition 2 therefore motivates treating the measurement operator as a fixed forward solve rather than describing an active computation path.

C. AEPS-PINN Network Architecture

AEPS-PINN uses a dual-head network with a shared trunk, a five-layer multilayer perceptron (MLP) with 64 tanh neurons per layer (17,986 parameters in total). The coordinates (x, y) are first mapped by a fixed Fourier feature encoding with B = 4 geometrically spaced bands, Eq. (19) [29], [30], with $\omega_0 = 1.0$ and $\omega_b \in \{1, 2, 4, 8\}$, giving an 18-dimensional input ($2 + 4B$) and a 64-dimensional trunk output $\mathbf{h}$.

$$\begin{aligned} \varphi(x,y) &= [x,\, y,\, \gamma_b(x),\, \gamma_b(y)]_{b=0}^{B-1}, \\ \gamma_b(s) &= [\sin(\omega_b s),\, \cos(\omega_b s)], \\ \omega_b &= \omega_0\, 2^b \end{aligned} \tag{19}$$

The potential head is a single linear layer, Eq. (20) [19], [40]. The conductivity head is a linear layer with pre-activation z followed by a bounded sigmoid that keeps the conductivity within $[\sigma_{\min}, \sigma_{\max}] = [0.5, 5.5]$, Eq. (21) [40], where sig(·) denotes the logistic function.

$$u(x,y) = \mathbf{w}_u^{\top}\mathbf{h} + b_u \tag{20}$$

$$\begin{aligned} \hat{\sigma}(x,y) &= \sigma_{\min} + (\sigma_{\max} - \sigma_{\min})\text{sig}(z), \\ z &= \mathbf{w}_\sigma^{\top}\mathbf{h} + b_\sigma \end{aligned} \tag{21}$$

Because the sigmoid derivative vanishes for strongly negative z, a straight-through estimator (STE) replaces it in the backward pass with the constant in Eq. (22) [31], so that the head receives a full-strength gradient while the forward output remains bounded. Unlike an unbounded Softplus head, the lower bound

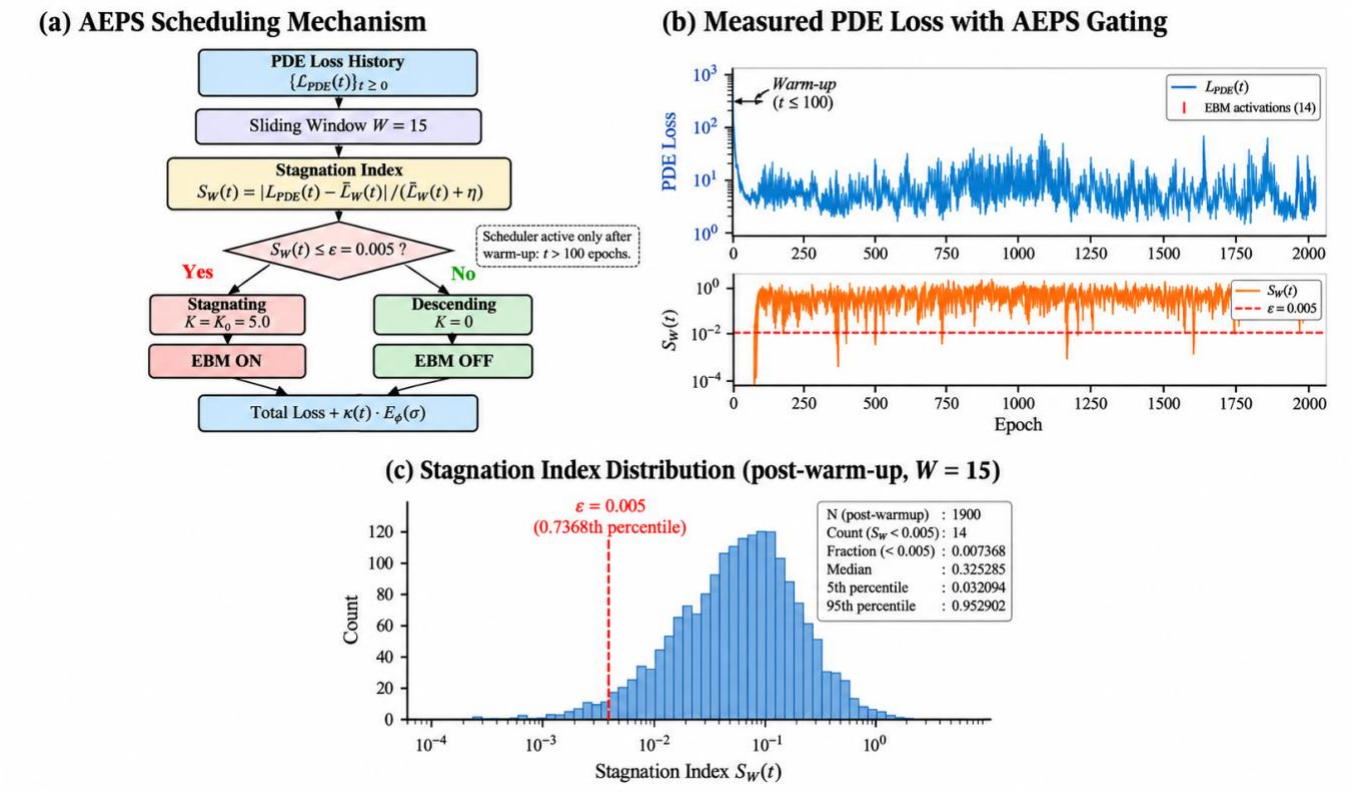


Fig. 3. Adaptive energy-prior scheduling behavior: (a) stagnation-based EBM activation mechanism, (b) PDE residual loss and corresponding EBM activation events during training, and (c) distribution of the stagnation index relative to the activation threshold $\varepsilon = 0.005$. Panel (b) also shows the stagnation index $S_W(t)$ for a representative run (seed 42, 14 activations), and panel (c) is computed over the post-warm-up epochs.

Manuscript received 14 August 2026; Accepted 16 October 2026; Available online 9 November 2026
Digital Object Identifier (**DOI**): https://doi.org/10.35882/jeeemi.v9i1.2012
Copyright © 2026 by the authors. This work is an open-access article and licensed under a Creative Commons Attribution-ShareAlike 4.0 International License (CC BY-SA 4.0).

$\sigma_{\min}$ = 0.5 also excludes the trivial solution $\sigma \approx 0$, for which the residual of Eq. (6) vanishes for any u.

$$\left.\frac{\partial \hat{\sigma}}{\partial z}\right|_{\text{backward}} = \sigma_{\max} - \sigma_{\min} = 5.0 \quad (22)$$

D. Physics-Informed Loss Formulation

The networks are trained with the composite objective of Eq. (23) [19], [26].

$$\mathcal{L} = \lambda_{\text{PDE}}\mathcal{L}_{\text{PDE}} + \lambda_{\text{Dir}}\mathcal{L}_{\text{Dir}} + \lambda_{\text{meas}}\mathcal{L}_{\text{meas}} + \lambda_{\sigma\text{bnd}}\mathcal{L}_{\sigma\text{bnd}} + \lambda_{\text{bg}}\mathcal{L}_{\text{bg}} + \kappa(t)\,E_{\phi}(\hat{\sigma}) \quad (23)$$

The first five terms are applied at every step with fixed weights; the multiplier $\kappa(t)$ of the energy prior E_ϕ is set to 0 or κ_0 by the scheduler of Section II.E, and when $\kappa(t)$ = 0 the EBM is not evaluated. The PDE term (λ_{PDE} = 1.0) is the mean squared residual at M = 10,000 interior collocation points, Eq. (24) [19]. The measurement term (λ_{meas} = 1000) is the mean squared error between the predicted and measured boundary potentials at N_b = 256 points $\mathbf{x}_b$, Eq. (25) [19], [20], where u_{meas} is obtained from the forward solve.

$$\mathcal{L}_{\text{PDE}} = \frac{1}{M}\sum_{i=1}^{M} |r(x_i, y_i)|^2 \quad (24)$$

$$\mathcal{L}_{\text{meas}} = \frac{1}{N_b}\sum_{b=1}^{N_b} \left(u(\mathbf{x}_b) - u_{\text{meas}}(\mathbf{x}_b)\right)^2 \quad (25)$$

The Dirichlet term (λ_{Dir} = 200) penalizes deviation of the predicted boundary potential from the homogeneous solution of Eq. (10); the conductivity-boundary term ($\lambda_{\sigma\text{bnd}}$ = 100) penalizes deviation of the boundary conductivity from σ_0 = 1.0; and the background-anchor term (λ_{bg} = 200) constrains the conductivity to σ_0 outside an inclusion mask. This mask is derived from the ground-truth phantom (cells deviating from σ_0 by more than 10^{-3}, dilated by 0.06 domain units, i.e., four grid cells), so the anchor uses oracle information that is unavailable in practice. It is used deliberately as an upper-bound design that tests whether interior contrast can be recovered under ideal background suppression, and its influence is quantified by the ablation in Section III.F.

E. Adaptive Energy-Prior Scheduling

The AEPS mechanism activates the EBM regularizer only when the PDE residual stagnates. At each Adam epoch t, the scheduler computes the normalized deviation of the PDE loss from its mean over the last W

Algorithm 1. AEPS-PINN training and conductivity reconstruction

Input: collocation points (x_i, y_i), i = 1, …, M (M = 10,000); boundary points x_b with measurements u_{meas}, b = 1, …, N_b (N_b = 256); background mask; loss weights λ (Section II.D); scheduler parameters W, ε, κ_0, t_{warmup} (Section II.E); budgets T_A = 2,000 and T_L = 500.
Output: trained parameters θ^*; conductivity $\sigma(x, y; \theta^*)$ on the 12,644 interior cells.

Stage 1: Adam optimization with adaptive energy-prior scheduling

Initialize θ (Xavier uniform); load the pretrained EBM E_ϕ and freeze ϕ.
for t = 1, …, T_A do
  Encode (x, y) by Eq. (19); predict u and σ by Eqs. (20)–(21).
  Compute the residual $r(x, y)$ by automatic differentiation, Eq. (6).
  Evaluate L_{PDE} and L_{meas} (Eqs. (24)–(25)) and L_{Dir}, $L_{\sigma\text{bnd}}$, L_{bg} (Section II.D).
  Compute $S_W(t)$ by Eq. (26) and $\kappa(t)$ by Eq. (27).
  if $\kappa(t) > 0$ then
  $L \leftarrow L + \kappa(t)E_\phi(\sigma)$, Eq. (23)
  else
   skip the EBM forward pass (no autograd graph is built)
  end if
  Back-propagate with the STE, Eq. (22); clip the gradient norm at 1.0; Adam update (learning rate 10^{-3}).
end for

Stage 2: L-BFGS fine-tuning with the prior disabled

Set $\kappa \leftarrow 0$.
for s = 1, …, T_L do
  L-BFGS step on Eq. (23) (strong-Wolfe line search, history 50, max_iter 20).
  if the gradient or loss change is below 10^{-9} then break
end for
return θ^* and $\sigma(x, y; \theta^*)$

Manuscript received 14 August 2026; Accepted 16 October 2026; Available online 9 November 2026
Digital Object Identifier (**DOI**): https://doi.org/10.35882/jeeemi.v9i1.2012
Copyright © 2026 by the authors. This work is an open-access article and licensed under a Creative Commons Attribution-ShareAlike 4.0 International License (CC BY-SA 4.0).

Algorithm 2. Adaptive energy-prior schedule

Input: PDE loss $L_{PDE}(t)$ at Adam epoch t; window length $W = 15$; threshold $\varepsilon = 0.005$; prior weight $\kappa_0 = 5.0$; warm-up $t_{warmup} = 100$; $\eta = 10^{-8}$; frozen pretrained EBM E_ϕ (Section II.E); current conductivity prediction σ.
Output: prior weight $\kappa(t)$ and, when the gate opens, the prior term $\kappa(t)E_\phi(\sigma)$ of Eq. (23).
Executed at every Adam epoch t of Stage 1 (line 6 of Algorithm 1)

1: Append $L_{PDE}(t)$ to the loss history and retain its W most recent values.
2: Compute the window mean of L_{PDE} over the last W epochs, Eq. (26).
3: Compute the stagnation index $S_W(t)$, the normalized deviation of $L_{PDE}(t)$ from this mean, Eq. (26).
4: if $t > t_{warmup}$ and $S_W(t) < \varepsilon$ then
5: $\kappa(t) \leftarrow \kappa_0$, Eq. (27); evaluate $E_\phi(\sigma)$ on the 12,644 interior cells.
6: $L \leftarrow L + \kappa(t)E_\phi(\sigma)$, Eq. (23); the prior gradient propagates through the PINN trunk.
7: Record the activation (activation counts in Section III.B).
8: else
9: $\kappa(t) \leftarrow 0$; skip the EBM forward pass (no autograd graph is built).
10: end if
11: return $\kappa(t)$; the gate is re-evaluated at every epoch without a refractory period, and $\kappa \leftarrow 0$ throughout Stage 2.

Algorithm 3. Multi-harmonic EIT boundary-voltage simulation

Input: phantom σ on the 128 × 128 grid (12,644 interior cells, $\sigma_0 = 1.0$); amplitudes a_1–a_4 = 0.6, 0.4, 0.25, 0.15; $N_b = 256$ boundary points; $K = 5{,}000$ Jacobi sweeps; singular-value tolerances $\tau \in \{10^{-6}, 10^{-8}, 10^{-10}\}$.
Output: boundary measurement matrices V_e, RMS amplitudes, numerical ranks $\text{rank}_\tau(V_e)$, and the superposition residual.

Boundary-voltage simulation (Section III.A)

1: Define the excitation schemes e: single $m = 1$; single $m = 2$; superposed $m = 1$–4, Eq. (8); and the four harmonics $m = 1$–4 applied separately.
2: for each excitation scheme e do
3: for each current pattern $g_j(\theta)$ of scheme e do
4: Solve the discretized forward problem for $g_j(\theta)$ by K non-differentiable Jacobi sweeps, Eq. (16).
5: Sample the potential at the N_b boundary points to obtain the 1 × 256 row vector v_j.
6: end for
7: Stack the rows v_j into V_e (1 × 256 for one pattern; 4 × 256 for four separate injections).
8: end for

Measurement-rank analysis (Section III.E)

9: for each excitation scheme e do
10: Compute the RMS amplitude of each single-pattern measurement.
11: Compute the singular values $s_1 \geq s_2 \geq \ldots$ of V_e by singular value decomposition.
12: for each τ do compute $\text{rank}_\tau(V_e)$, the numerical rank of V_e at tolerance τ end for
13: end for
14: Superposition check: relative L2 difference $\|v_{sup} - \Sigma_m v_m\|_2 / \|v_{sup}\|_2$ between the superposed response and the sum of the four individual responses.
15: return V_e, the RMS amplitudes, $\text{rank}_\tau(V_e)$, and the superposition residual.

epochs, Eq. (26) [41], with $\eta = 10^{-8}$, and sets the prior weight by the gating rule of Eq. (27) [28], [41].

$$S_W(t) = \frac{|\mathcal{L}_{\text{PDE}}(t) - \bar{\mathcal{L}}_W(t)|}{\bar{\mathcal{L}}_W(t) + \eta}, \qquad \bar{\mathcal{L}}_W(t) = \frac{1}{W}\sum_{\tau=t-W+1}^{t} \mathcal{L}_{\text{PDE}}(\tau) \tag{26}$$

$$\kappa(t) = \begin{cases} \kappa_0, & t > t_{\text{warmup}},\ S_W(t) < \varepsilon \\ 0, & \text{otherwise} \end{cases} \tag{27}$$

A value of $S_W(t)$ above ε indicates that the PDE loss is still changing, so the prior is not needed; a value below ε indicates a plateau, and the prior is activated with κ_0 = 5.0 (Fig. 3(a)). After the warm-up, the gate opens if and only if $S_W(t) < \varepsilon$, with no refractory period or

Manuscript received 14 August 2026; Accepted 16 October 2026; Available online 9 November 2026
Digital Object Identifier (**DOI**): https://doi.org/10.35882/jeeemi.v9i1.2012
Copyright © 2026 by the authors. This work is an open-access article and licensed under a Creative Commons Attribution-ShareAlike 4.0 International License (CC BY-SA 4.0).

minimum spacing. When $\kappa(t) = 0$, the EBM forward pass is skipped, so no autograd graph is built for the prior; when the gate opens, the prior gradient propagates through the PINN trunk. The values $W = 15$, $\varepsilon = 0.005$, $\kappa_0 = 5.0$, and $t_{warmup} = 100$ were chosen empirically, and their sensitivity is analysed in Section III.G. The EBM [27] is a four-layer MLP that maps the flattened interior conductivity (12,644 values) through 128, 64, and 32 ReLU units to a scalar energy without input normalization; it has 1,628,929 parameters, 90.6 times as many as the PINN. It was pretrained with denoising score matching (DSM) [42] for 50 epochs on 1,000 synthetic phantoms with randomized inclusion number and conductivity, balanced by an equal number of negative samples (flat fields, uniform noise, and Gaussian perturbations), using Adam (learning rate 10^{-3}, weight decay 10^{-5}, cosine annealing, gradient clipping at 1.0), and then frozen. The DSM loss decreased by only 0.11%, and the energy gap between in- and out-of-distribution samples reached 2.59 against an intended margin of 5.0, so the prior landscape did not converge well. The evaluation phantom is not a pretraining sample but is in-distribution.

F. Two-Stage Optimization and Training Algorithm

Training proceeds in two stages (Algorithm 1). Stage 1 initializes the network parameters by Xavier uniform initialization [43] and applies Adam [32] for 2,000 epochs (learning rate 10^{-3}, gradient-norm clipping at 1.0) with the scheduler active; during this stage the PDE loss decreases from about 1,020 to a fluctuating range of 5–30. Stage 2 applies L-BFGS [33] for 500 steps (max_iter = 20, tolerance_grad = tolerance_change = 10^{-9}, strong-Wolfe line search [44], history size 50) with the prior permanently disabled to avoid loss-scale interference. This budget is identical for all configurations in the main comparison. The ablation and sensitivity studies use 2,000 Adam epochs and 100 L-BFGS steps, which still exceeds the point of diminishing returns because only 2 of the 500 L-BFGS steps improve the loss (Section III.C). Algorithm 1 specifies the inputs, initialization, loss evaluation, stagnation computation, gating decision, optimizer transition, stopping criteria, and outputs, together with the corresponding equations. The stagnation-gated activation of the energy prior in lines 6–11 of Algorithm 1 is detailed in Algorithm 2, and the multi-harmonic boundary-voltage simulation and measurement-rank analysis used in Sections III.A and III.E are summarized in Algorithm 3.

III. Results

A. Experimental Setup and Evaluation Protocol

All experiments used a fixed three-inclusion phantom on a 128 × 128 Cartesian grid within the unit disk (12,644 interior cells) with a background conductivity of $\sigma_0 = 1.0$. Inclusion 1 (conductive, $\sigma = 5.0$) is centred at (−0.5238, 0.2117) with radius 0.2217, inclusion 2 (resistive, $\sigma = 0.5$) at (0.4225, 0.2840) with radius 0.2451, and inclusion 3 (conductive, $\sigma = 5.0$) at (0.1248, −0.5414) with radius 0.0756. Reconstruction used $M = 10{,}000$ interior collocation points and $N_b = 256$ boundary points, and the boundary data were generated by 5,000 Jacobi sweeps under the excitation of Eq. (8), as summarized in Algorithm 3. Three configurations shared the phantom, architecture, loss weights, excitation, and background anchor: the Standard PINN (no prior), the Static EBM-PINN (prior applied at every step with $\kappa = 5.0$), and AEPS-PINN (Eq. (27)). Each was trained with the budget of Section II.F (2,000 Adam epochs and 500 L-BFGS steps) for five seeds with the same initialization scheme and stopping criteria; the run manifests confirm identical phantom geometry and EBM checksum. One Standard PINN run (seed 44) diverged to NaN and is reported as a failed run rather than replaced, giving $n = 4$, 5, and 5 valid runs. The ablation and sensitivity studies (Sections III.F, III.G, and III.I) used 2,000 Adam epochs and 100 L-BFGS steps, identical within each study. All runs used PyTorch 2.13.0 on a CPU with a fixed thread count. Reconstruction quality was evaluated over the interior cells by the MSE, RMSE, relative L2 error, PSNR = $20 \log_{10}(5.0/\text{RMSE})$, and SSIM [45] computed on the interior mask with a dynamic range matched to the ground truth. Because these global metrics can be favourable for a near-uniform prediction, inclusion recovery was assessed by the Dice coefficient [46] and Intersection-over-Union (IoU) [47] between the thresholded prediction and each ground-truth inclusion mask, together with the mean predicted conductivity and the recovered contrast in each inclusion. Results are reported as mean ± SD with the number of valid runs n; 95% confidence intervals (CIs) are computed as mean ± $t_{0.975,\, n-1} \cdot \text{SD}/\sqrt{n}$, and differences between configurations are tested with paired Wilcoxon signed-rank [48] and paired t-tests.

B. AEPS Scheduling Behavior

Over the 2,500 steps of each AEPS-PINN run, the EBM was evaluated 15 ± 4 times ($n = 5$), i.e., in 0.60% ± 0.16% of all steps and in 0.79% ± 0.21% of the 1,900 post-warm-up Adam epochs in which the scheduler was active. The Static EBM-PINN evaluated the EBM 7,511 ± 353 times, once per Adam epoch and per L-BFGS closure call, so the scheduler reduced prior evaluations by 99.8%. For the representative seed 42, the post-warm-up stagnation index had a median of 0.325, a 5th percentile of 0.032, and a 95th percentile of 0.953; $\varepsilon = 0.005$ lies at its 0.74th percentile, and exactly 14 of the 1,900 values fell below it, matching the 14 recorded activations (Fig. 3(b)–(c)). The gate

Manuscript received 14 August 2026; Accepted 16 October 2026; Available online 9 November 2026
Digital Object Identifier (**DOI**): https://doi.org/10.35882/jeeemi.v9i1.2012
Copyright © 2026 by the authors. This work is an open-access article and licensed under a Creative Commons Attribution-ShareAlike 4.0 International License (CC BY-SA 4.0).

Table 1. Comparative reconstruction accuracy, inclusion-level recovery, and computational efficiency of Standard PINN, Static EBM-PINN, and AEPS-PINN under equivalent optimization budgets. Results are expressed as mean ± standard deviation and 95% confidence intervals where applicable.

Metric	Standard PINN (n = 4)	Static EBM-PINN (n = 5)	AEPS-PINN (n = 5)
MSE	0.9127 ± 0.0084 [0.8993, 0.9261]	0.8967 ± 0.0085 [0.8861, 0.9073]	0.9008 ± 0.0108 [0.8874, 0.9142]
RMSE	0.9553 ± 0.0044 [0.9483, 0.9623]	0.9469 ± 0.0045 [0.9413, 0.9525]	0.9491 ± 0.0057 [0.9420, 0.9562]
Relative L2 error	0.6330 ± 0.0029 [0.6284, 0.6376]	0.6274 ± 0.0030 [0.6237, 0.6311]	0.6288 ± 0.0038 [0.6241, 0.6335]
PSNR (dB)	14.38 ± 0.04 [14.32, 14.44]	14.45 ± 0.04 [14.40, 14.50]	14.43 ± 0.05 [14.37, 14.49]
SSIM (interior-masked)	0.8690 ± 0.0005 [0.8682, 0.8698]	0.8610 ± 0.0031 [0.8572, 0.8648]	0.8680 ± 0.0006 [0.8673, 0.8687]
Dice / IoU	0 / 0	0 / 0	0 / 0
Inclusion 1 (σ = 5.0): mean predicted σ (contrast)	0.9724 (1.004)	0.9832 (0.996)	0.9930 (1.006)
Inclusion 2 (σ = 0.5): mean predicted σ (contrast)	0.9517 (0.983)	1.0578 (1.071)	0.9830 (0.996)
Inclusion 3 (σ = 5.0): mean predicted σ (contrast)	0.9623 (0.994)	1.0182 (1.031)	0.9932 (1.006)
Detected inclusions (all runs)	0 / 12	0 / 15	0 / 15
Wall-clock time (s)	1,909.7 ± 202.9	1,774.5 ± 177.5	1,719.0 ± 219.3
EBM evaluations	0	7,511 ± 353	15 ± 4
EBM time (s); share of run time	0; 0%	51.37 ± 5.11; 2.90%	0.116 ± 0.031; 0.01%
Peak resident memory (MB)[a]	775.1	775.3	772.0

[a] *Measured separately with 2,000 Adam epochs + 20 L-BFGS steps; the EBM checkpoint is loaded in all three configurations.*

therefore responds to the lower tail of a fluctuating quantity rather than to sustained plateaus of the PDE loss.

Table 2. Comparison of boundary measurement-matrix rank and RMS voltage amplitude for single-harmonic, superposed multi-harmonic, and separately injected harmonic excitation schemes.

Excitation scheme	Matrix size	Rank	RMS amplitude
Single m = 1 (a_1 = 0.6)	1 × 256	1	0.528
Single m = 2 (a_2 = 0.4)	1 × 256	1	0.454
Superposed m = 1–4 (this study)	1 × 256	1	0.904
Four harmonics injected separately	4 × 256	4	–

C. Conductivity Reconstruction Performance

Table 1 summarizes reconstruction quality, inclusion-level recovery, and computational cost under the equal budget. The mean MSE was 0.9127 for the Standard PINN (n = 4), 0.8967 for the Static EBM-PINN (n = 5), and 0.9008 for AEPS-PINN (n = 5); the corresponding PSNR values were 14.38, 14.45, and 14.43 dB. The 95% CIs of MSE, RMSE, relative L2 error, and PSNR overlap for all three configurations. Relative to the Standard PINN, AEPS-PINN changed MSE by −0.0119 (−1.3%) and PSNR by +0.05 dB; relative to the Static EBM-PINN, it changed MSE by +0.0041 (+0.5%). For AEPS-PINN versus the Standard PINN, the paired Wilcoxon test gives p = 0.125, the minimum attainable with four pairs, whereas the paired t-test gives p = 0.011 under a normality assumption that four differences cannot verify; the difference is therefore not regarded as established, and its magnitude is small relative to the reconstruction error itself. The only metric whose CIs separate is the masked SSIM, which is 0.007–0.008 lower for the Static EBM-PINN than for the other two configurations; because SSIM is dominated by the background (Section III.D), this difference does not indicate a difference in structural recovery. Continuous application of the prior thus did not degrade the error metrics.

The L-BFGS stage contributed little: across all runs, only 2 of the 500 L-BFGS steps improved the total loss, with stagnation from step 3, and the remaining steps were strong-Wolfe line-search evaluations without an

Manuscript received 14 August 2026; Accepted 16 October 2026; Available online 9 November 2026
Digital Object Identifier (**DOI**): https://doi.org/10.35882/jeeemi.v9i1.2012
Copyright © 2026 by the authors. This work is an open-access article and licensed under a Creative Commons Attribution-ShareAlike 4.0 International License (CC BY-SA 4.0).

improving direction. The principal verified benefit of AEPS-PINN is therefore not accuracy but the 99.8% reduction in prior evaluations at statistically indistinguishable error (Section III.H).

D. Inclusion-Level Reconstruction

The inclusion-level rows of Table 1 quantify this. In every run of every configuration, Dice and IoU were 0 for all three inclusions, and centroid errors are undefined because no predicted region crossed the detection threshold. Predicted conductivity remained within approximately 0.71–1.16 against a true range of 0.5–5.0, and the mean predicted conductivity in each inclusion was 0.95–1.06, giving recovered contrast ratios of 0.98–1.07 against true ratios of 5.0 and 0.5. Inclusions of opposite polarity were not distinguished: their mean predicted values differ by at most 0.021 for the Standard PINN, 0.010 for AEPS-PINN, and 0.075 for the Static EBM-PINN, which even places the resistive inclusion slightly above the background (recovered contrast 1.071). The global metrics of Table 1 therefore do not reflect recovery of the interior structure by any configuration.

E. Excitation Sensitivity and Measurement Rank

The analytical modal sensitivity of the configured excitation at $r_0 = 0.5$ is 10.1 times that of a single $m = 2$ mode (Eq. (13)), and the measured boundary RMS amplitude is 1.99 times larger (0.904 versus 0.454). To test whether this gain corresponds to more information, the numerical rank of the boundary measurement matrix, i.e., the number of its singular values that remain non-negligible at a prescribed tolerance [49], was computed for four excitation schemes on the same phantom by Algorithm 3 (Table 2). The superposed four-harmonic injection yields rank 1, as does any single harmonic, whereas four separately injected harmonics yield rank 4. The rank is unchanged at singular-value tolerances of 10^{-6}, 10^{-8}, and 10^{-10}, and the superposed measurement equals the sum of the four individual responses to within a relative L2 difference of 5.10×10^{-7}.

F. Background-Anchor Ablation

Because the anchor mask is derived from the phantom being reconstructed, its weight was varied over $\lambda_{bg} \in \{200, 10, 0\}$ (two seeds each, 2,000 Adam epochs and 100 L-BFGS steps). The mean MSE was 0.8980 ± 0.0163, 0.9657 ± 0.0106, and 1.0079 ± 0.0464 for λ_{bg} = 200, 10, and 0, so removing the anchor increased MSE by 12% and reduced masked SSIM from 0.8679 to 0.8471, consistently across both seeds. With $n = 2$, however, the 95% CI half-width of the MSE exceeds 0.14 and the minimum attainable exact Wilcoxon p-value is 0.50, so the difference is a consistent trend rather than an established effect.

Table 3. Sensitivity of reconstruction MSE and EBM activation count to AEPS scheduler parameters (seed 42; 2,000 Adam epochs, 100 L-BFGS steps, W=15, epsilon=0.005, kappa_0=5, warm-up=100)

Parameter	Value	EBM activations	MSE
Default	see text	14	0.9096
ε	0.001	4	0.9104
	0.01	34	0.9068
	0.05	147	0.9059
W	5	20	0.9079
	30	17	0.9162
	50	14	0.9067
κ_0	1.0	9	0.9077
	10.0	17	0.9072
t_{warmup}	0	20	0.9097
	300	14	0.9096

Table 4. Effects of additive Gaussian boundary-measurement noise on reconstruction accuracy and adaptive EBM activation under different signal-to-noise ratios

η_n	SNR (dB)	MSE (mean ± SD) [95% CI]	SSIM (masked)	AEPS activations
0.00	∞	0.8990 ± 0.0117 [0.8699, 0.9281]	0.8678 ± 0.0002	14.3 ± 4.5
0.01	40.0	0.9053 ± 0.0109 [0.8782, 0.9324]	0.8677 ± 0.0009	20.7 ± 3.2
0.03	30.5	0.9023 ± 0.0078 [0.8829, 0.9217]	0.8684 ± 0.0007	17.0 ± 3.6
0.05	26.0	0.9010 ± 0.0020 [0.8960, 0.9060]	0.8689 ± 0.0011	21.0 ± 3.5

Manuscript received 14 August 2026; Accepted 16 October 2026; Available online 9 November 2026
Digital Object Identifier (**DOI**): https://doi.org/10.35882/jeeemi.v9i1.2012
Copyright © 2026 by the authors. This work is an open-access article and licensed under a Creative Commons Attribution-ShareAlike 4.0 International License (CC BY-SA 4.0).

The anchor does not conceal a better reconstruction: Dice and IoU are 0 in all settings, and the predicted ranges (0.726–1.044, 0.647–0.984, and 0.635–1.056) span less than 10% of the true range. Without the anchor, the mean prediction moves away from the truth (0.990, 0.856, and 0.832 for λ_{bg} = 200, 10, and 0), because the measurement term alone, acting on rank-1 boundary data, does not constrain the interior. The anchor therefore acts as a regularizer, and the metrics in Table 1 are upper bounds of what is achievable without oracle information.

G. Scheduler Sensitivity

Each scheduler parameter was varied around the default (W = 15, ε = 0.005, κ_0 = 5.0, t_{warmup} = 100) with the others fixed (eleven configurations, seed 42, 2,000 Adam epochs and 100 L-BFGS steps; Table 3); this is a single-seed trend analysis without significance testing. The activation count is governed almost entirely by ε, rising from 4 at ε = 0.001 to 147 at ε = 0.05 (36.8-fold), whereas κ_0 (1.0–10.0), W (5–50), and t_{warmup} (0–300) change it by factors of 1.9, 1.4, and 1.4. The setting t_{warmup} = 300 is identical to the default because the first activation occurs at epoch 384. Reconstruction quality is insensitive to all four parameters: the MSE ranges from 0.9059 to 0.9162 (coefficient of variation 1.1%) while the activation count varies 37-fold, Dice and IoU are 0 everywhere, and the predicted conductivity range width is 0.279–0.333, compared with 4.5 for the ground truth.

This sensitivity follows from the distribution of the stagnation index (Fig. 3(c)): over the 1,900 post-warm-up epochs it ranges from 3.3×10^{-5} to 2.57 (median 0.325), and its density rises steeply just above ε, so that small increases in ε admit many additional epochs. Two consequences follow. The reduction in prior evaluations does not require careful threshold tuning because quality is unchanged across the tested range; however, the activation count itself is specific to the threshold and should not be interpreted as a property of the method.

H. Computational Performance

Under the equal budget of 2,500 steps (Table 1), the mean wall-clock time was 1,909.7 ± 202.9 s for the Standard PINN, 1,774.5 ± 177.5 s for the Static EBM-PINN, and 1,719.0 ± 219.3 s for AEPS-PINN. Identical configurations varied by up to 24% between executions because of machine load, so these differences lie within run-to-run variability, and AEPS-PINN is not slower than the baseline. The EBM-evaluation count, which is deterministic, is the more reliable efficiency measure: 7,511 ± 353 evaluations (51.37 ± 5.11 s, 2.90% of the run time) for the Static EBM-PINN versus 15 ± 4 evaluations (0.116 ± 0.031 s, 0.01%) for AEPS-PINN. End-to-end time is dominated by the L-BFGS stage rather than by the prior. Peak resident memory, measured separately with 2,000 Adam epochs and 20 L-BFGS steps, was 772–775 MB for all configurations (baseline process 196 MB), because the EBM checkpoint is loaded in all three; this does not imply that the EBM has no memory cost.

I. Noise Sensitivity

Additive Gaussian noise was applied once to the boundary data before training and held fixed, Eq. (28) [50], where $\xi \sim N(0, \mathbf{I})$ and $\eta_n \in \{0, 0.01, 0.03, 0.05\}$ (three seeds each, 2,000 Adam epochs and 100 L-BFGS steps); the achieved signal-to-noise ratios were 40.0, 30.5, and 26.0 dB (Table 4).

$$u_{\text{noisy}} = u_{\text{meas}} + \eta_n \parallel u_{\text{meas}} \parallel_{\text{RMS}} \xi \tag{28}$$

The mean MSE varied between 0.8990 and 0.9053 (a 0.7% spread). and the masked SSIM between 0.8677 and 0.8689, non-monotonically and without significant differences under paired Wilcoxon and t-tests; the predicted range remained approximately [0.71, 1.04]. With n = 3, the minimum attainable Wilcoxon p-value is 0.25 and the 95% CI half-widths of the MSE are 0.005–0.029, so only large effects are detectable. This insensitivity must not be read as noise robustness: Dice and IoU are already 0 without noise, so there is no recovered structure for noise to degrade. The one measurable effect is on the scheduler, whose mean activation count rose from 14.3 at η_n = 0 to 20.7 and 21.0 at η_n = 0.01 and 0.05 (about 45%), consistent with a detector that responds to loss fluctuations rather than to plateaus (Section III.G).

IV. Discussion

A. Interpretation of AEPS-PINN Performance

Under equal optimization budgets, AEPS-PINN neither improves nor degrades the reconstruction error relative to the baselines: its MSE differs from that of the Standard PINN by −1.3% and from that of the Static EBM-PINN by +0.5%, with overlapping 95% CIs (Table 1). The change is cost: the prior is evaluated 15 ± 4 instead of 7,511 ± 353 times (−99.8%) and accounts for 0.01% instead of 2.90% of the run time. The equivalence of the Static EBM-PINN and AEPS-PINN implies that, in this configuration, most evaluations under continuous application were unnecessary rather than harmful. Because the EBM was triggered only by lower-tail fluctuations of the stagnation index and was itself not well converged, the results establish stagnation gating as a cheaper, quality-neutral alternative to continuous application, not as a means of improving accuracy; whether gated priors help under more informative measurements remains open.

B. Excitation, Measurement Rank, and Identifiability

The multi-harmonic excitation increases the aggregate modal sensitivity at r_0 = 0.5 by a factor of 10.1 relative to a single m = 2 mode and the measured boundary amplitude by a factor of 1.99, potentially improving the

Manuscript received 14 August 2026; Accepted 16 October 2026; Available online 9 November 2026
Digital Object Identifier (**DOI**): https://doi.org/10.35882/jeeemi.v9i1.2012
Copyright © 2026 by the authors. This work is an open-access article and licensed under a Creative Commons Attribution-ShareAlike 4.0 International License (CC BY-SA 4.0).

Table 5. Comparison of representative electrical impedance tomography reconstruction frameworks

Study	Method	Evaluation setting and excitation	Reported quantitative results	Training data and compute	Main contribution / limitation
Hamilton and Hauptmann (2018) [14]	Deep D-bar (D-bar + U-Net)	Simulated ACT4 (32 electrodes, trigonometric voltage patterns) and KIT4 (16 electrodes, adjacent current patterns); experimental tank tests	Mean relative ℓ_2 error on 16 simulated test samples: 28.05% → 9.92% (ACT4), 16.82% → 9.12% (KIT4)	4,096 simulated pairs per system; ≈4 h training (one GPU); 7.65 ms per image	Real-time deblurring of D-bar images without experimental training data; errors from in-distribution simulations
Hamilton *et al.* (2019) [15]	Beltrami-net (D-bar + CNN)	Experimental ACT4 and KIT4 tank data (electrodes and patterns as above)	SSIM 0.696–0.730, rel. ℓ_2 13.3–21.0% (ACT4); SSIM 0.827–0.892, rel. ℓ_2 13.1–17.3% (KIT4)	4,096 / 15,360 simulated pairs; ≈3 h per network (one GPU)	Domain-independent learning validated on experimental data; needs a full set of current patterns
Pokkunuru *et al.* (2023) [28]	PINN with continuous EBM prior	Simulated EIT; K excitation patterns with internal potential data [23]	PINN convergence more than 10× faster with the prior	Prior evaluated at every step; K + 1 networks for K patterns [23]	Reference for energy-prior regularization; relies on internal data unavailable in boundary-only EIT
Yang *et al.* (2025) [23]	Two-stage CNN–PINN	Full inverse; simulated 16-electrode EIT (four-electrode protocol); test data at 20 dB SNR	SSIM / CC / RIE: 0.4066 / 0.7043 / 0.9365 (Case 1); 0.3671 / 0.4030 / 2.4903 (Case 2); 0.4036 / 0.7146 / 0.4954 (Case 3)	10,000 samples; CNN ≈5 h + ≈1 h per PINN session (two GPUs)	CNN supplies internal potentials to the PINN; needs supervised training data
Smyl *et al.* (2025) [21]	PINN-EIT	Experimental difference imaging of damaged composite truss (16 electrodes, adjacent) and airfoil (20 electrodes)	≈8 × 10^4-fold faster inference than classical inversion; SSIM/MSE not reported	5 × 10^4 simulated samples per case; training ≈5× that of a data-driven NN	Better damage localization with fewer artifacts; higher training complexity
Yang *et al.* (2026) [24]	Physics-embedded dual learning (CNN + PINN)	Full inverse; simulation and water tank; 16 electrodes, moving excitation; 128 × 128 grid	SSIM 0.355–0.742 (simulation), 0.373–0.631 (water tank)	15,000 samples; 7,000–10,000 training iterations	Data-driven and physics-embedded learning with water-tank validation; needs supervised training data
Zhu *et al.* (2026) [25]	PGCT-PINN	CT-derived lung EIT simulation and phantom experiments	SSIM 0.9644; RE 0.0548 (data-limited conditions)	Data-limited training; 16 frames/s on a Raspberry Pi	Cooperative physics-guided training with phantom and embedded validation
AEPS-PINN (this study)	Adaptive EBM-PINN	Full inverse, boundary data only; synthetic 2D phantom (128 × 128); one composite four-harmonic injection (rank 1)	MSE 0.9008; rel. L2 0.629; Dice = IoU = 0; ≈99.8% fewer EBM evaluations than the Static EBM-PINN	No paired data for the PINN (EBM: 1,000 phantoms); 1,719 ± 219 s per reconstruction (CPU)	Lower EBM cost without loss of quality; inclusions not recovered (rank-1 measurement)

SSIM, CC, RIE, and relative errors are not directly comparable across studies, which differ in phantoms, conductivity contrast, domain, and metric definitions; the masked SSIM of the present study (0.868) reflects a near-uniform prediction and is therefore not listed. Compute figures refer to GPU training except for the present study

signal-to-noise ratio under amplitude-independent noise conditions. It does not increase information: by linearity of the forward problem, the superposed measurement equals the sum of the four individual

Manuscript received 14 August 2026; Accepted 16 October 2026; Available online 9 November 2026
Digital Object Identifier (**DOI**): https://doi.org/10.35882/jeeemi.v9i1.2012
Copyright © 2026 by the authors. This work is an open-access article and licensed under a Creative Commons Attribution-ShareAlike 4.0 International License (CC BY-SA 4.0).

responses. The corresponding boundary-voltage response matrix has rank 1 for the single superposed injection, whereas the matrix formed from four separately applied injection patterns has rank 4 (Table 2).

The rank-1 measurement matrix indicates that the superposed multi-harmonic excitation constitutes a single independent current-injection pattern, rather than four independent measurements. Although this configuration provides multiple boundary voltage samples, it offers less excitation diversity than separately applied harmonic patterns. Combined with the depth-dependent decay of interior sensitivity [5], this limited measurement diversity may contribute to the unsuccessful inclusion recovery observed across the evaluated EBM strategies, random seeds, background-anchor weights, noise levels, and scheduler settings. However, the present experiments do not establish measurement rank as the sole cause of reconstruction failure. The results therefore do not support a claim that superposed multi-harmonic excitation improves reconstruction accuracy; increasing excitation diversity requires multiple independent current-injection patterns [4], [10]. Accordingly, the global metrics in Table 1 should be interpreted cautiously, since favourable MSE, PSNR, and SSIM values for nearly uniform predictions do not demonstrate successful recovery of interior conductivity structures.

C. Comparison with Related EIT and PINN Studies

Table 5 compares AEPS-PINN with seven representative EIT reconstruction studies. Because these studies differ in phantoms and data, excitation patterns, evaluation protocols, metric definitions, and computing platforms, the comparison is in terms of setting and order of magnitude rather than ranking. Three differences are decisive. First, data and excitation: the D-bar-based networks [14], [15] and the hybrid CNN–PINN frameworks [23], [24] use 16–32 electrodes with multiple current or voltage patterns, i.e., measurements of rank well above one, whereas the present study uses a single composite injection of rank 1; the EBM-prior PINN of Pokkunuru *et al.* [28], like the formulation of Bar and Sochen [20], additionally relies on internal potential data and on one network per excitation pattern [23], neither of which is available here. Second, reconstruction error: the directly comparable metric is the relative ℓ_2 error, which is 9.1–9.9% for Deep D-bar on simulated test data [14] and 13.1–21.0% for Beltrami-net on experimental tank data [15], against 62.9% for AEPS-PINN. Studies that recover inclusions report SSIM values of 0.355–0.742 in simulation, 0.373–0.631 on water-tank data [24] and 0.367–0.407 under 20 dB noise [23], and PGCT-PINN reports an SSIM of 0.9644 with a relative error of 0.0548 [25]. The masked SSIM of AEPS-PINN (0.868) is not comparable to these values because it reflects a near-uniform prediction over a background-dominated domain, which is why Dice and IoU, reported by none of the comparison studies, are needed to expose the failure. Third, computational requirements: the supervised and hybrid approaches need 4,096–50,000 simulated training samples [14], [15], [21], [23], [24] and GPU training of about 3–5 h [14], [15], [23], after which inference is fast, from 7.65 ms per image [14] to 16 frames/s on an embedded platform [25] and about 8×10^4 times faster than classical inversion [21]; AEPS-PINN needs no paired training data for the PINN but solves each reconstruction by per-instance optimization (1,719 ± 219 s on a CPU). Finally, Pokkunuru *et al.* reported that a continuously applied EBM prior accelerates PINN convergence more than tenfold in a setting with internal potential data [28]; the present study did not test convergence speed in that setting, but shows that in a boundary-only, rank-1 setting, gating the prior preserves the quality of continuous application with 99.8% fewer evaluations, whereas no prior can compensate for the missing measurement information. The comparison thus indicates that the reconstruction failure reported here reflects the information content of the measurement rather than a deficiency specific to the scheduler.

D. Limitations

The measurement is based on a single superposed current-injection pattern (rank 1), which limits excitation diversity compared with multiple independent injection patterns, regardless of the optimizer used (Section III.E). The stagnation index is a noisy lower-tail detector: $\varepsilon = 0.005$ lies at the 0.74th percentile of its post-warm-up distribution, and the activation count varies 37-fold with ε (Section III.G). The EBM prior was not well converged (DSM loss reduced by 0.11%, energy gap 2.59 against a margin of 5.0) and is 90.6 times larger than the PINN, and the Born-approximation sensitivity analysis is only qualitative for the 5:1 contrast phantom. The homogeneous-reference boundary penalty may also bias the predicted boundary potential toward the homogeneous solution, and its independent effect on reconstruction accuracy was not evaluated in this study.

All results come from one synthetic, in-distribution phantom on a 128 × 128 grid with two to five seeds per condition, so effects smaller than a few percent cannot be resolved, and the scheduler sensitivity analysis uses a single seed. The background anchor uses oracle mask information, so metrics obtained with it are upper bounds (Section III.F). Only additive Gaussian noise was tested; electrode and forward-model mismatch were not evaluated because no structure is recovered even under matched, noiseless conditions. No experimental phantom or measured biomedical data were used, and each reconstruction requires about 30

Manuscript received 14 August 2026; Accepted 16 October 2026; Available online 9 November 2026
Digital Object Identifier (**DOI**): https://doi.org/10.35882/jeeemi.v9i1.2012
Copyright © 2026 by the authors. This work is an open-access article and licensed under a Creative Commons Attribution-ShareAlike 4.0 International License (CC BY-SA 4.0).

min of per-instance optimization on a CPU, so neither clinical reliability nor real-time operation is demonstrated.

E. Implications and Requirements for Biomedical Application

For PINN-based EIT, the results indicate that a learned prior need not be active throughout optimization: the Static EBM-PINN and AEPS-PINN reach statistically indistinguishable error metrics despite a roughly 500-fold difference in prior evaluations. Stagnation-gated activation is therefore a viable way to contain the cost of expensive auxiliary priors, and the principle can be transferred to other PDE-constrained inverse problems. The present results do not, however, support claims of clinically reliable imaging. Before biomedical applicability can be claimed, five requirements must be met: (1) multiple independent current-injection patterns, so that the rank of the measurement matrix exceeds the number of unknown structures [4], [10]; (2) a realistic electrode configuration modelled with the complete electrode model, including contact impedance and discrete electrode positions [9]; (3) evaluation of model mismatch in boundary shape, electrode position, and contact impedance; (4) validation on experimental tank phantoms with measured voltages [15], [24]; and (5) final validation on measured biomedical data against a reference modality [3]. Within the computational setting, next steps include a better-conditioned stagnation indicator, such as an exponentially smoothed relative loss decrement, a training-level comparison of single and multi-harmonic excitation under independent injections, and higher-resolution or finite-element formulations. Real-time or embedded deployment would additionally require amortized inference, because the present per-instance optimization is dominated by the L-BFGS stage rather than by the prior.

V. Conclusion

This study developed AEPS-PINN, a PINN framework for EIT in which an energy-based prior is activated only when the PDE residual stagnates, and evaluated it under equal optimization budgets. AEPS-PINN reached a mean MSE of 0.9008 (95% CI 0.8874–0.9142, n = 5), statistically indistinguishable from the Standard PINN (0.9127, n = 4) and the Static EBM-PINN (0.8967, n = 5), while reducing EBM evaluations by 99.8%, from 7,511 ± 353 to 15 ± 4 per run, without loss of reconstruction quality. No configuration recovered the inclusions: Dice and IoU were zero in every run, and the predicted conductivity spanned less than 10% of the true range. The superposed multi-harmonic excitation yields a rank-1 boundary-voltage response matrix, indicating limited excitation diversity despite a 1.99-fold increase in boundary-signal amplitude. This limitation may contribute to the unsuccessful inclusion recovery, although the present experiments do not isolate its effect from other methodological factors. The verified contribution is therefore a quality-neutral, low-cost prior-scheduling mechanism together with a quantitative identifiability analysis of single-injection EIT. Future work should evaluate AEPS-PINN with multiple independent current-injection patterns, a better-conditioned stagnation indicator, realistic electrode models, and experimental phantom data.

Declarations

Ethics Approval and Consent to Participate

This study was conducted entirely through computational simulations and numerical experiments involving synthetic electrical impedance tomography (EIT) data. No human participants, animals, identifiable personal information, or clinical interventions were involved. Therefore, institutional ethical approval and informed consent to participate were not required.

Consent for Publication

Not applicable. This manuscript does not contain identifiable personal information, individual participant data, or images requiring consent for publication.

Competing Interests

The authors declare that they have no financial, commercial, professional, or personal competing interests that could have influenced the design, execution, analysis, interpretation, or reporting of this research.

Funding

This research received no specific grant from any funding agency in the public, commercial, or not-for-profit sectors.

Data Availability Statement

The datasets used in this study were generated through computational simulations based on the electrical impedance tomography configurations and experimental parameters described in the manuscript. These include synthetic conductivity phantoms, simulated boundary-voltage measurements, and numerical reconstruction results. The data supporting the findings of this study are available from the corresponding author upon reasonable request.

Code Availability

The computational framework was implemented using Python and PyTorch and includes the electrical impedance tomography forward simulation, AEPS-PINN architecture, adaptive energy-prior scheduling, and numerical evaluation procedures. The source code, trained model parameters, configuration files, and

Manuscript received 14 August 2026; Accepted 16 October 2026; Available online 9 November 2026
Digital Object Identifier (**DOI**): https://doi.org/10.35882/jeeemi.v9i1.2012
Copyright © 2026 by the authors. This work is an open-access article and licensed under a Creative Commons Attribution-ShareAlike 4.0 International License (CC BY-SA 4.0).

reproducibility scripts are available from the corresponding author upon reasonable request.

Author Contributions

Dikky Juliyanto contributed to the conceptualization, methodology, software development, computational experiments, formal analysis, investigation, visualization, and preparation of the original manuscript draft. Endah Rahmawati contributed to research supervision, methodological guidance, interpretation of findings, and critical review and editing of the manuscript.

Declaration of Generative Artificial Intelligence and AI-Assisted Technologies

During the preparation of this manuscript, the authors used Claude (Anthropic) to assist reference formatting. All content was reviewed, verified, and revised by the authors, who take full responsibility for the scientific content, methods, results, and conclusions of this work.

Research Integrity and Originality

The authors affirm that the manuscript presents original research, has not been published previously, and is not currently under consideration for publication elsewhere. All relevant sources have been appropriately acknowledged and cited. The authors confirm that the reported computational experiments, numerical results, and interpretations accurately represent the research conducted and that no data fabrication, falsification, or inappropriate manipulation has occurred.

Acknowledgments

The authors express their appreciation to the Department of Physics, Universitas Negeri Surabaya (UNESA), Indonesia, for providing academic support, research facilities, and a conducive research environment.

References

[1] M. Cheney, D. Isaacson, and J. C. Newell, “Electrical impedance tomography,” *SIAM Review*, vol. 41, no. 1, pp. 85–101, 1999, doi: 10.1137/S0036144598333613.

[2] L. Borcea, “Electrical impedance tomography,” *Inverse Problems*, vol. 18, no. 6, pp. R99–R136, 2002, doi: 10.1088/0266-5611/18/6/201.

[3] A. Adler and A. Boyle, “Electrical impedance tomography: Tissue properties to image measures,” *IEEE Transactions on Biomedical Engineering*, vol. 64, no. 11, pp. 2494–2504, 2017, doi: 10.1109/TBME.2017.2728323.

[4] D. Isaacson, “Distinguishability of conductivities by electric current computed tomography,” *IEEE Transactions on Medical Imaging*, vol. 5, no. 2, pp. 91–95, 1986, doi: 10.1109/TMI.1986.4307752.

[5] H. Garde and K. Knudsen, “Distinguishability revisited: Depth dependent bounds on reconstruction quality in electrical impedance tomography,” *SIAM Journal on Applied Mathematics*, vol. 77, no. 2, pp. 697–720, 2017, doi: 10.1137/16M1072991.

[6] A. Adler and W. R. B. Lionheart, “Uses and abuses of EIDORS: An extensible software base for EIT,” *Physiological Measurement*, vol. 27, no. 5, pp. S25–S42, 2006, doi: 10.1088/0967-3334/27/5/S03.

[7] A. Adler *et al.*, “GREIT: A unified approach to 2D linear EIT reconstruction of lung images,” *Physiological Measurement*, vol. 30, no. 6, pp. S35–S55, 2009, doi: 10.1088/0967-3334/30/6/S03.

[8] A. Borsic, B. M. Graham, A. Adler, and W. R. B. Lionheart, “In vivo impedance imaging with total variation regularization,” *IEEE Transactions on Medical Imaging*, vol. 29, no. 1, pp. 44–54, 2010, doi: 10.1109/TMI.2009.2022540.

[9] E. Somersalo, M. Cheney, and D. Isaacson, “Existence and uniqueness for electrode models for electric current computed tomography,” *SIAM Journal on Applied Mathematics*, vol. 52, no. 4, pp. 1023–1040, 1992, doi: 10.1137/0152060.

[10] D. G. Gisser, D. Isaacson, and J. C. Newell, “Electric current computed tomography and eigenvalues,” *SIAM Journal on Applied Mathematics*, vol. 50, no. 6, pp. 1623–1634, 1990, doi: 10.1137/0150096.

[11] A. Hauptmann, F. Lucka, M. Betcke, N. Huynh, J. Adler, B. Cox, P. Beard, S. Ourselin, and S. Arridge, “Model-based learning for accelerated, limited-view 3-D photoacoustic tomography,” *IEEE Transactions on Medical Imaging*, vol. 37, no. 6, pp. 1382–1393, 2018, doi: 10.1109/TMI.2018.2820382.

[12] K. H. Jin, M. T. McCann, E. Froustey, and M. Unser, “Deep convolutional neural network for inverse problems in imaging,” *IEEE Transactions on Image Processing*, vol. 26, no. 9, pp. 4509–4522, 2017, doi: 10.1109/TIP.2017.2713099.

[13] S. Arridge, P. Maass, O. Öktem, and C.-B. Schönlieb, “Solving inverse problems using data-driven models,” *Acta Numerica*, vol. 28, pp. 1–174, 2019, doi: 10.1017/S0962492919000059.

[14] S. J. Hamilton and A. Hauptmann, “Deep D-bar: Real-time electrical impedance tomography imaging with deep neural networks,” *IEEE Transactions on Medical Imaging*, vol. 37, no. 10, pp. 2367–2377, 2018, doi: 10.1109/TMI.2018.2828303.

[15] S. J. Hamilton, A. Hänninen, A. Hauptmann, and V. Kolehmainen, “Beltrami-net: Domain-independent deep D-bar learning for absolute

Manuscript received 14 August 2026; Accepted 16 October 2026; Available online 9 November 2026
Digital Object Identifier (**DOI**): https://doi.org/10.35882/jeeemi.v9i1.2012
Copyright © 2026 by the authors. This work is an open-access article and licensed under a Creative Commons Attribution-ShareAlike 4.0 International License (CC BY-SA 4.0).

imaging with electrical impedance tomography (a-EIT)," *Physiological Measurement*, vol. 40, no. 7, Art. no. 074002, 2019, doi: 10.1088/1361-6579/ab21b2.

[16] M. Capps and J. L. Mueller, "Reconstruction of organ boundaries with deep learning in the D-bar method for electrical impedance tomography," *IEEE Transactions on Biomedical Engineering*, vol. 68, no. 3, pp. 826–833, 2021, doi: 10.1109/TBME.2020.3006175.

[17] R. Guo and J. Jiang, "Construct deep neural networks based on direct sampling methods for solving electrical impedance tomography," *SIAM Journal on Scientific Computing*, vol. 43, no. 3, pp. B678–B711, 2021, doi: 10.1137/20M1367350.

[18] T. Zhang *et al.*, "Advances of deep learning in electrical impedance tomography image reconstruction," *Frontiers in Bioengineering and Biotechnology*, vol. 10, Art. no. 1019531, 2022, doi: 10.3389/fbioe.2022.1019531.

[19] M. Raissi, P. Perdikaris, and G. E. Karniadakis, "Physics-informed neural networks: A deep learning framework for solving forward and inverse problems involving nonlinear partial differential equations," *Journal of Computational Physics*, vol. 378, pp. 686–707, 2019, doi: 10.1016/j.jcp.2018.10.045.

[20] L. Bar and N. Sochen, "Strong solutions for PDE-based tomography by unsupervised learning," *SIAM Journal on Imaging Sciences*, vol. 14, no. 1, pp. 128–155, 2021, doi: 10.1137/20M1332827.

[21] D. Smyl, T. N. Tallman, L. Homa, C. Flournoy, S. J. Hamilton, and J. Wertz, "Physics informed neural networks for electrical impedance tomography," *Neural Networks*, vol. 188, Art. no. 107410, 2025, doi: 10.1016/j.neunet.2025.107410.

[22] S. Soelistiono, "Deep physics-informed neural network (D-PINN) for real-time dynamic electrical impedance tomography (EIT) reconstruction with geometrical uncertainty robustness," *Indonesian Applied Physics Letters*, vol. 6, no. 1, pp. 30–36, 2025, doi: 10.20473/iapl.v6i1.84060.

[23] X. Yang, Y. Zhang, H. Chen, G. Ma, and X. Wang, "A two-stage imaging framework combining CNN and physics-informed neural networks for full-inverse tomography: A case study in electrical impedance tomography (EIT)," *IEEE Signal Processing Letters*, vol. 32, pp. 1096–1100, 2025, doi: 10.1109/LSP.2025.3545306.

[24] X. Yang, Y. Zhang, H. Chen, G. Ma, and X. Wang, "A physics-embedded dual-learning imaging framework for electrical impedance tomography," *Neural Networks*, vol. 197, Art. no. 108464, 2026, doi: 10.1016/j.neunet.2025.108464.

[25] Z. Zhu, Z. Zhang, Z. Wang, Z. Yuan, X. Zhao, A. Ma, J. Sun, L. Xu, and L. Mo, "PGCT-PINN: A physics-guided cooperative training framework for enhanced resolution and consistency in lung EIT imaging," *IEEE Internet of Things Journal*, vol. 13, no. 8, pp. 17631–17642, 2026, doi: 10.1109/JIOT.2026.3662909.

[26] S. Wang, Y. Teng, and P. Perdikaris, "Understanding and mitigating gradient flow pathologies in physics-informed neural networks," *SIAM Journal on Scientific Computing*, vol. 43, no. 5, pp. A3055–A3081, 2021, doi: 10.1137/20M1318043.

[27] Y. LeCun, S. Chopra, R. Hadsell, M. Ranzato, and F. J. Huang, "A tutorial on energy-based learning," in *Predicting Structured Data*, G. Bakır, T. Hofmann, B. Schölkopf, A. J. Smola, B. Taskar, and S. V. N. Vishwanathan, Eds. Cambridge, MA, USA: MIT Press, 2006.

[28] A. Pokkunuru, P. Rooshenas, T. Strauss, A. Abhishek, and T. Khan, "Improved training of physics-informed neural networks using energy-based priors: A study on electrical impedance tomography," in *Proc. International Conference on Learning Representations (ICLR)*, 2023. [Online]. Available: https://openreview.net/pdf?id=zqkfJA6R1-r

[29] B. Mildenhall, P. P. Srinivasan, M. Tancik, J. T. Barron, R. Ramamoorthi, and R. Ng, "NeRF: Representing scenes as neural radiance fields for view synthesis," *Communications of the ACM*, vol. 65, no. 1, pp. 99–106, 2022, doi: 10.1145/3503250.

[30] S. Wang, H. Wang, and P. Perdikaris, "On the eigenvector bias of Fourier feature networks: From regression to solving multi-scale PDEs with physics-informed neural networks," *Computer Methods in Applied Mechanics and Engineering*, vol. 384, Art. no. 113938, 2021, doi: 10.1016/j.cma.2021.113938.

[31] I. Hubara, M. Courbariaux, D. Soudry, R. El-Yaniv, and Y. Bengio, "Quantized neural networks: Training neural networks with low precision weights and activations," *Journal of Machine Learning Research*, vol. 18, no. 187, pp. 1–30, 2018. [Online]. Available: https://jmlr.org/papers/v18/16-456.html

[32] R.-Y. Sun, "Optimization for deep learning: An overview," *Journal of the Operations Research Society of China*, vol. 8, no. 2, pp. 249–294, 2020, doi: 10.1007/s40305-020-00309-6.

[33] D. C. Liu and J. Nocedal, "On the limited memory BFGS method for large scale optimization," *Mathematical Programming*, vol. 45, no. 1–3, pp. 503–528, 1989, doi: 10.1007/BF01589116.

Manuscript received 14 August 2026; Accepted 16 October 2026; Available online 9 November 2026
Digital Object Identifier (**DOI**): https://doi.org/10.35882/jeeemi.v9i1.2012
Copyright © 2026 by the authors. This work is an open-access article and licensed under a Creative Commons Attribution-ShareAlike 4.0 International License (CC BY-SA 4.0).

[34] J. L. Mueller and S. Siltanen, *Linear and Nonlinear Inverse Problems with Practical Applications*, Computational Science & Engineering, vol. 10. Philadelphia, PA, USA: SIAM, 2012, doi: 10.1137/1.9781611972344.

[35] G. E. Karniadakis, I. G. Kevrekidis, L. Lu, P. Perdikaris, S. Wang, and L. Yang, "Physics-informed machine learning," *Nature Reviews Physics*, vol. 3, no. 6, pp. 422–440, 2021, doi: 10.1038/s42254-021-00314-5.

[36] A. Griewank and A. Walther, *Evaluating Derivatives: Principles and Techniques of Algorithmic Differentiation*, 2nd ed. Philadelphia, PA, USA: SIAM, 2008, doi: 10.1137/1.9780898717761.

[37] W. R. B. Lionheart, "EIT reconstruction algorithms: Pitfalls, challenges and recent developments," *Physiological Measurement*, vol. 25, no. 1, pp. 125–142, 2004, doi: 10.1088/0967-3334/25/1/021.

[38] Y. Saad, *Iterative Methods for Sparse Linear Systems*, 2nd ed. Philadelphia, PA, USA: SIAM, 2003.

[39] N. J. Higham, *Accuracy and Stability of Numerical Algorithms*, 2nd ed. Philadelphia, PA, USA: SIAM, 2002.

[40] I. Goodfellow, Y. Bengio, and A. Courville, *Deep Learning*. Cambridge, MA, USA: MIT Press, 2016.

[41] L. Prechelt, "Early stopping — But when?," in *Neural Networks: Tricks of the Trade*, 2nd ed., G. Montavon, G. B. Orr, and K.-R. Müller, Eds., Lecture Notes in Computer Science, vol. 7700. Berlin, Germany: Springer, 2012, pp. 53–67, doi: 10.1007/978-3-642-35289-8_5.

[42] P. Vincent, "A connection between score matching and denoising autoencoders," *Neural Computation*, vol. 23, no. 7, pp. 1661–1674, 2011, doi: 10.1162/NECO_a_00142.

[43] X. Glorot and Y. Bengio, "Understanding the difficulty of training deep feedforward neural networks," in *Proc. 13th International Conference on Artificial Intelligence and Statistics (AISTATS)*, Proceedings of Machine Learning Research, vol. 9, 2010, pp. 249–256.

[44] J. Nocedal and S. J. Wright, *Numerical Optimization*, 2nd ed. New York, NY, USA: Springer, 2006, doi: 10.1007/978-0-387-40065-5.

[45] Z. Wang, A. C. Bovik, H. R. Sheikh, and E. P. Simoncelli, "Image quality assessment: From error visibility to structural similarity," *IEEE Transactions on Image Processing*, vol. 13, no. 4, pp. 600–612, 2004, doi: 10.1109/TIP.2003.819861.

[46] D. Müller, I. Soto-Rey, and F. Kramer, "Towards a guideline for evaluation metrics in medical image segmentation," *BMC Research Notes*, vol. 15, Art. no. 210, 2022, doi: 10.1186/s13104-022-06096-y.

[47] L. Maier-Hein *et al.*, "Metrics reloaded: Recommendations for image analysis validation," *Nature Methods*, vol. 21, no. 2, pp. 195–212, 2024, doi: 10.1038/s41592-023-02151-z.

[48] F. Wilcoxon, "Individual comparisons by ranking methods," *Biometrics Bulletin*, vol. 1, no. 6, pp. 80–83, 1945, doi: 10.2307/3001968.

[49] G. H. Golub and C. F. Van Loan, *Matrix Computations*, 4th ed. Baltimore, MD, USA: Johns Hopkins University Press, 2013.

[50] J. Kaipio and E. Somersalo, *Statistical and Computational Inverse Problems*, Applied Mathematical Sciences, vol. 160. New York, NY, USA: Springer, 2005, doi: 10.1007/b138659.

Author Biography



Dikky Juliyanto is a student in the Physics Study Program, State University of Surabaya (UNESA), Surabaya, Indonesia. Alongside his physics training, he has a strong interest in technology, particularly application and web development, which he pursues through independent learning and freelance and personal software projects. He applies the analytical, systematic, and problem-solving skills developed in physics to the design, implementation, and optimization of computational tools, including the AEPS-PINN framework developed in this study. He aims to become a professional developer of innovative, functional, and socially beneficial digital solutions.



Dr. Endah Rahmawati, S.T., M.Si., received the B.Eng. degree in Physics Engineering from the Sepuluh Nopember Institute of Technology (ITS), Surabaya, Indonesia, in 2003, and the M.Si. degree in Physics from the Institut Teknologi Bandung (ITB), Bandung, Indonesia, in 2009. She received her Ph.D. degree from the University of Brawijaya, Malang, Indonesia, in 2025, with research focused on Electrical Impedance Tomography (EIT). She is currently a lecturer in the Department of Physics, Faculty of Mathematics and Natural Sciences, Universitas Negeri Surabaya (Unesa), Indonesia. Her research interests include Electrical Impedance Tomography (EIT), impedance spectroscopy, and biophysics instrumentation.

Manuscript received 14 August 2026; Accepted 16 October 2026; Available online 9 November 2026
Digital Object Identifier (**DOI**): https://doi.org/10.35882/jeeemi.v9i1.2012
Copyright © 2026 by the authors. This work is an open-access article and licensed under a Creative Commons Attribution-ShareAlike 4.0 International License (CC BY-SA 4.0).